

Low-Bremsstrahlung X-Ray Source Using a Low-Voltage High-Current-Density Nanostructured Field Emission Cathode and a Transmission Anode for Markerless Soft Tissue Imaging

Shuo Cheng, Frances Ann Hill, Eric Vincent Heubel, and Luis Fernando Velásquez-García, *Senior Member, IEEE*

Abstract—We report the design, fabrication, and proof-of-concept characterization of an X-ray generator for improved X-ray absorption imaging that uses a nanostructured field emission cathode as the electron source and a microstructured transmission anode as the X-ray generating structure. Field emission cathodes consume less power, respond faster, and tolerate lower vacuum than the thermionic cathodes used in conventional X-ray generators. The use of a transmission anode, instead of a conventional reflection anode, allows filtering of the background radiation (bremsstrahlung) while allowing efficient generation of X-ray at lower voltages by exciting atomic shell transitions, resulting in emission of X-ray with narrow spectral linewidth for sharper imaging of biological tissue. The fabricated field emission cathode contains arrays of self-aligned and gated silicon field emitters. The field emission cathodes turn on at bias voltages as low as 25 V, and their gates transmit almost 100% of the electrons to the anode. The cathodes produce per-emitter electron currents in excess of 2 μA (current density $>2\text{ A/cm}^2$) at a bias voltage of 80 V. A desktop rig is built to generate X-ray with a field emission cathode and transmission anode. Using the facility, we obtained X-ray absorption images of several objects. The images clearly show details under 500 μm in size, as well as soft tissue and fine bone structures without using contrast agents. [2014-0087]

Index Terms—Field emission, medical imaging, X-ray generation.

I. INTRODUCTION

MICRO AND nanoelectromechanical systems (MEMS and NEMS, respectively) for X-ray applications such as

Manuscript received March 19, 2014; revised June 16, 2014; accepted June 17, 2014. Date of publication July 22, 2014; date of current version March 31, 2015. This work was supported by the Defense Advanced Research Projects Agency under Grant N66001-11-4204, Subaward 219877, through the Massachusetts General Hospital. Subject Editor A. Luque.

S. Cheng was with the Microsystems Technology Laboratories, Massachusetts Institute of Technology, Cambridge, MA 02139 USA. He is now with Stellarray, Inc., Austin, TX 78754 USA (e-mail: cheng.s.eric@gmail.com).

F. A. Hill was with the Microsystems Technology Laboratories, Massachusetts Institute of Technology, Cambridge, MA 02139 USA. She is now with KLA-Tencor, Milpitas, CA 95035 USA (e-mail: fahill@alum.mit.edu).

E. V. Heubel is with the Department of Mechanical Engineering, Massachusetts Institute of Technology, Cambridge, MA 02139 USA (e-mail: evheubel@mit.edu).

L. F. Velásquez-García is with the Microsystems Technology Laboratories, Massachusetts Institute of Technology, Cambridge, MA 02139 USA (e-mail: velasquez@alum.mit.edu).

Color versions of one or more of the figures in this paper are available online at <http://ieeexplore.ieee.org>.

Digital Object Identifier 10.1109/JMEMS.2014.2332176

detection [1]–[4], optics [5], and generation [6]–[8] have been reported. X-ray sources play an important role in applications such as medical imaging, industrial inspection, transportation safety, and scientific research. X-ray generation technology developed over a century ago is still used today in the majority of commercial X-ray sources. A typical X-ray source consists of a thermionic cathode and a reflection anode inside of a vacuum chamber that has an X-ray transmission window. The cathode generates a beam of electrons that is accelerated towards the anode; depending on the application, the bias voltage on the anode is from a few kilovolts to over a hundred kilovolts above the bias voltage of the cathode. Electrons emitted by the cathode collide with the anode and convert their kinetic energy into X-ray radiation, a fraction of which escapes the vacuum chamber through a transmission window made of a suitable material, such as beryllium. The X-ray emission is a mix of bremsstrahlung radiation (broad, continuous spectrum) and characteristic radiation—a signature of the material that is emitting the X-ray (i.e., emission at specific wavelengths corresponding to atomic shell transitions of electrons) [9]. This article is the extended version of a recent report on an X-ray source composed of a nanostructured silicon field emission cathode and a transmission anode with micrometer-thick X-ray generating material that achieves emission of X-ray with narrow spectral linewidth for markerless imaging of biological samples [10].

A. X-Ray Cathodes

In a thermionic cathode electrons are “boiled” off the surface of a hot filament (heated to a temperature greater than 1100 K) when the energy of the electrons is sufficient to overcome the potential barrier holding the electrons within the material. Thermionic cathodes have a number of issues including low power efficiency due to the filament heating, low brightness, slow response, and quick degradation of the filament when exposed to relatively low vacuum and/or reactive residual gasses [11]; field emission cathodes are an attractive alternative to thermionic cathodes that relaxes these limitations [12]. Field emission cathodes use high surface electric fields ($>3 \times 10^7\text{ V/cm}$ [13]) to decrease and narrow the potential barrier that traps electrons within the emitting material, causing electrons to tunnel to vacuum. As shown in

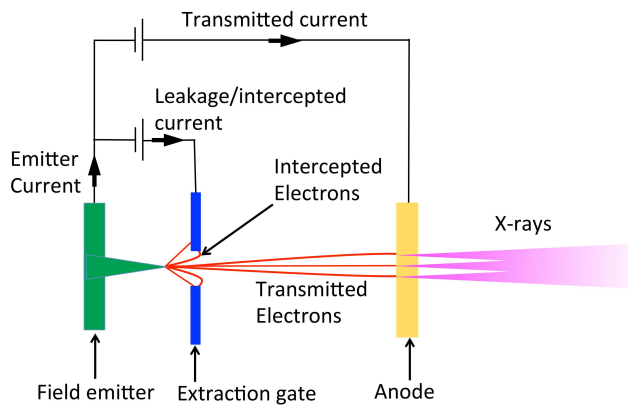


Fig. 1. Illustration of an X-ray generator with a field emission cathode and a transmission anode.

Figure 1, a field emission cathode consists of one or more sharp protrusions, i.e., emitters, facing one or more electrode gates. A positive bias voltage with respect to the bias voltage of the emitters is applied to the extraction gate to extract electrons from the emitter tips. The emitters have tip radii from several nanometers to tens of nanometers so that high electric fields on the tip surface are attained at low voltage. The gates have apertures that transmit a fraction of the electron current emitted. Between the emitter tips and the gates there is a dielectric layer or vacuum. The maximum current per emitter is dependent on factors such as the electrical conductivity of the emitters, the aspect ratio of the emitters, heat dissipation, and the maximum gate-to-emitter bias voltage before breakdown through the dielectric or vacuum. Field emitter arrays (FEAs) are implemented to increase the total emission current, emission uniformity, and reliability of the cathode.

Various materials have been explored for manufacturing field emitters. Carbon nanotube (CNT)-based field emission cathodes have been recently used in X-ray generators [14]–[18]. The cathodes are composed of a substrate with a CNT forest and a gate electrode bonded to the substrate. It is relatively simple to fabricate CNT forests, and the CNTs have small tip radii and high aspect ratio to, in principle, field emit electrons at low voltage. However, the separation between the gate and the emitter tips is generally large (on the order of 1 mm), the CNTs are tightly packed, the location of the CNTs is random, the height and diameter of the CNTs vary with a wide distribution, and a cluster of CNTs share the same gate aperture, resulting in high operating voltages (>500 V) and non-uniform current emission across the CNT forest. Also, a large portion of electrons emitted from the CNTs is intercepted by the gate, which decreases the efficiency of the cathode. The intercepted electrons could also cause outgassing when colliding with the gate, which lowers the vacuum surrounding the CNTs [19].

Spindt field emission cathodes are arrays of metallic field emitters with self-aligned extractor gate integrated to each emitter tip, which alleviates the high-voltage and low-transmission problems of the CNT forest-based cathodes [20].

The Spindt emitters are batch microfabricated by evaporating metal (typically molybdenum or tungsten) at an angle onto a rotating substrate with pre-fabricated gate apertures; the emitters have conic structure because of the shadowing effect of the aperture. These devices operate at low voltage (<100 V) because of the small gate-to-tip distance and the small emitter tip diameter. However, metal field emitters have lifetime issues as they quickly degrade when exposed to relatively low partial pressures of oxygen ($\sim 5 \times 10^{-7}$ Torr) [21].

Silicon field emitters have been investigated over the past few decades, primarily for field emission display applications [22]–[33]. Similar to Spindt emitters, silicon emitters have proximal gates for low turn-on voltage and high electron transmission efficiency. However, unlike Spindt tips, silicon tips can be operated in the supply-limited regime because of the wide tunability of the electrical conductivity of silicon through doping; operating the emitters in the supply-limited regime could be used to increase and uniformize the current emitted by the FEA [31]–[33]. FEAs reported in the literature have maximum per-emitter current of 0.1–0.5 $\mu\text{A}/\text{tip}$ [22], [28]–[30], and average current densities similar to those of CNT forest field emission cathodes (0.2–4 A/cm^2) [34]–[36]. In addition, unlike metal field emitters and thermionic emitters, silicon emitters can operate at lower vacuum and are resilient to residual oxygen [37], which makes them more compatible with portable applications. This paper reports a nanostructured silicon FEA that turns-on with as little as 25 V and produces per-emitter currents in excess of 2 μA (2 A/cm^2) with near 100% transmission efficiency; the higher performance is achieved using a fabrication process that yields a-few-microns-tall nanosharp emitters with proximal self-aligned submicron gate apertures. High-current emission is important for X-ray imaging applications because a high emission current reduces the exposure time, which reduces the blurring of the image.

B. Monochromatic X-Ray Generation

Monochromaticity of the X-ray has proven to be an important factor for high image quality [18], [38]–[43]. Conventional X-ray imaging systems use the broadband bremsstrahlung radiation to expose the object, resulting in blurry images. However, generation of purely monochromatic X-ray requires either high-energy electron sources [38], [40] or expensive precision optics [39]. X-ray filtering techniques can also be used to remove some of the unwanted frequency contents from the X-ray spectrum [41]–[43]; however, these techniques require certain peripheral structures that complicate the overall system. A simple approach for achieving monochromatic X-ray is reported in [18] where the anode voltage is set to a certain value such that the relative magnitude of the L-shell transition is maximized; a quasi-monochromatic X-ray at 2.45 kV energy is generated from a reflection molybdenum anode. Although the monochromaticity of the X-ray is highly desirable, such low-energy X-ray are not useful for medical imaging. In this paper, a transmission gold anode is used to take advantage of the inherent filtering capability of the gold film and the anode substrate. While

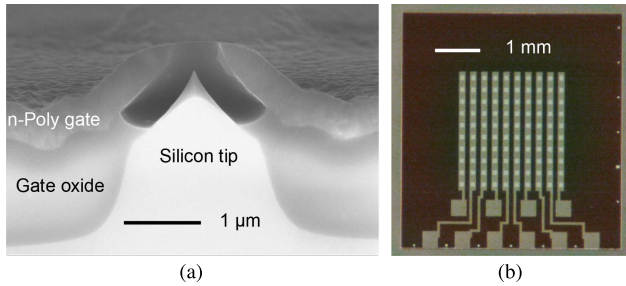


Fig. 2. (a) Cross-section of a gated silicon field emitter, (b) picture of a full field emitter array chip.

the achieved X-ray spectrum is dichromatic, the relatively high energy level of the radiation peaks (around 10 keV), the close proximity in wavelength of the two peaks, and the low bremsstrahlung emission at the anode bias voltages used in the experiments (15 - 40 kV) enable capturing very clear images of soft tissues without using contrast agents.

II. DEVICE DESIGN AND FABRICATION

A. Cathode Design and Fabrication

Figure 2(a) shows a scanning electron microscope (SEM) image of the cross-section of a gated silicon field emitter. The emitter consists of an n-silicon tip $2.5 \mu\text{m}$ tall with a 5 nm tip radius, a $1.5 \mu\text{m}$ thick gate oxide layer, and a 500 nm thick n-doped polysilicon gate with a $0.6 \mu\text{m}$ diameter aperture. The separation between the gate aperture and the tip is about $0.5 \mu\text{m}$. Figure 2(b) shows an optical microscope image of the whole FEA chip. The chip consists of a 10×10 array of electron guns with square packing and a pitch of $300 \mu\text{m}$. Each electron gun contains a 7×7 array of field emitters arranged in square packing with $10 \mu\text{m}$ pitch. Each column of 10 electron guns can be independently turned on, such that activation of a column results in the operation of 490 field emitters at once. The plurality of electron gun sets that can be individually actuated results in cathode redundancy and therefore, higher X-ray source reliability.

Figure 3 shows a set of SEM images that illustrates the process flow to fabricate the field emission cathode chip. The process is similar to those reported in [22]–[28] with a few modifications. The cathodes are fabricated on a 6" n-type silicon wafer ($1 \Omega\text{-cm}$ resistivity) with a film stack consisting of a 100 nm -thick thermal oxide film, a 100 nm -thick silicon-rich silicon nitride film and a 500 nm -thick chemical vapor deposited (CVD) oxide film. The silicon nitride layer between the two oxide layers functions as a diffusion barrier for a later process step. The film stack is dry etched to form $2.2 \mu\text{m}$ diameter discs (Figure 3(a)); each disc functions as an etch mask for one emitter. The silicon substrate is first etched using a sulfur hexafluoride (SF_6)-based isotropic dry etch to undercut the discs and form partially sharpened tips with $200\text{-}300 \text{ nm}$ diameter. A chlorine-based anisotropic dry etch further etches the exposed silicon to increase the height of the emitters (Figure 3(b)); this serves the purpose of increasing the thickness of the gate oxide layer so that the device can withstand larger bias voltages without breakdown. In the

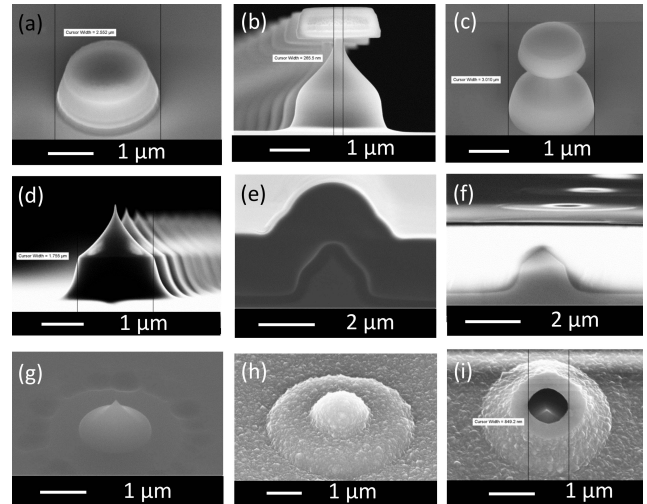


Fig. 3. (a)-(i) Sequential images of the fabrication process flow to create the gated field emitters.

next step, thermal oxidization is performed to fully sharpen the emitter tips to around 10 nm in diameter (Figure 3(c)); the tip sharpening step is different from [22], [26], [28] in that the oxidation is performed before removing the caps, which protects the top of the emitters from oxidizing because of the silicon nitride film. After the oxidation, the nitride and oxide films are then stripped using diluted hydrofluoric acid and hot phosphoric acid (Figure 3(d)), completing the fabrication of the emitters. The next steps create the self-aligned extractor gates with apertures. First, $4 \mu\text{m}$ of CVD oxide is deposited to completely cover the tips (Figure 3(e)). This oxide layer is densified by annealing in nitrogen for 30 minutes at 950°C , and then planarized using chemical mechanical polishing (CMP) (Figure 3(f)). A buffered oxide etch (BOE) is used to etch back the oxide layer just until the emitter tips are exposed (Figure 3(g)). Then, the emitters are coated with a $0.5 \mu\text{m}$ -thick CVD oxide layer. The different oxide thicknesses over the different areas of the emitters are chosen to achieve both high breakdown voltage as well as low turn-on voltage. Next, a 500 nm -thick n-doped polysilicon film (Figure 3(h)) is deposited as the gate material, and the substrate is polished using CMP to form the gate apertures and expose the gate oxide. The polysilicon film is patterned to form the gate strips, contact pads, and to electrically isolate emitters that are not part of the same column. Finally, a BOE dip is performed to etch the oxide immediately surrounding the emitter tips (Figure 3(i)). This opens the gates and removes the thin oxide layer surrounding the tips.

B. Description of the Transmission Anode

The anode is a 1" diameter $300 \mu\text{m}$ -thick beryllium wafer that has a $2.5 \mu\text{m}$ -thick evaporated gold film on one side. In a transmission anode, electrons impact an X-ray-generating film that is thick enough to absorb most of the electrons, but thin enough to avoid reabsorbing the majority of the X-ray produced (transmission anodes are designed for a particular anode voltage). A thick transmission anode could also help

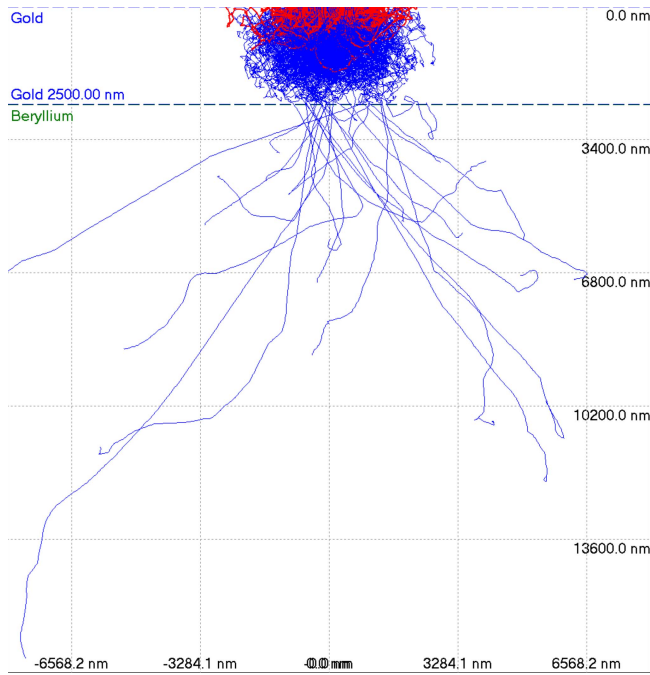


Fig. 4. Simulation of the trajectory of 1000 electrons as they travel through the anode structure using the 2D Monte Carlo simulation software CASINO. The trajectory of the backscattered electrons is shown in red while the trajectories of the electrons that stop inside the anode structure are shown in blue.

reduce the background radiation and improve the contrast of the images [9]. If the anode voltage is between the first and the second ionization potentials of the atomic shell transitions of the X-ray generating material (K-shell and L-shell), the radiation spectra will be mainly composed of the atomic shell transition peak that corresponds to the L-shell characteristic energy, resulting in emission of X-ray with narrow spectral linewidth for sharper imaging of low-Z materials [18]. In many X-ray generating materials, these peaks are of low enough energy that the supporting substrate in a transmission anode helps attenuate the background radiation surrounding peak emission. Using the software CASINO developed by the Universite de Sherbrooke [44], we conducted 2D Monte Carlo simulations of the interaction between the high-energy electrons and the anode structure to determine the thickness of the X-ray generating material. At 60 kV, i.e., the maximum anode bias voltage in our setup (see Section III.B), a 2.5 μm -thick gold film absorbs the great majority of the electrons (Figure 4) and the majority of the X-ray produced by the anode are not reabsorbed (Figure 5).

In a transmission anode, the X-ray that are transmitted through the anode plate are used for imaging; this is different from most X-ray sources, which are based on reflection anodes where a portion of the reflected X-ray is used. The X-ray generating surface of a reflection anode is slightly inclined with respect to the faraway direction of the incoming electrons, i.e., cathode-anode axis, to reduce the effective focal spot of the X-ray beam and to steer a fraction of the photons off-axis to be transmitted outside the vacuum chamber. Unfortunately, because of the orientation of the X-ray generating surface, reflection anodes are affected by the so-called heel effect,

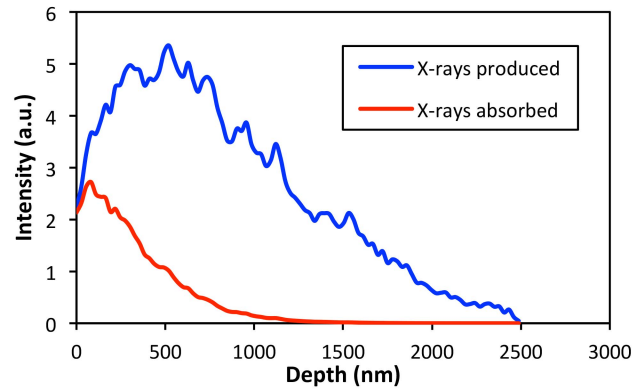


Fig. 5. Emitted and absorbed X-ray vs. anode depth from a simulation of the interaction of 1000 electrons with the anode structure using the 2D Monte Carlo simulation software CASINO.

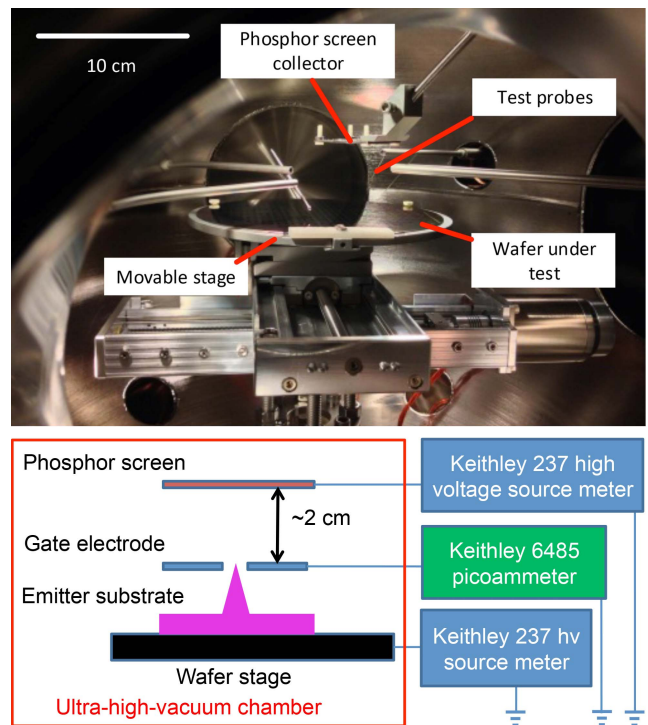


Fig. 6. Picture (top) and schematic (bottom) of the cathode testing rig.

i.e., a gradient in the intensity of the X-ray due to absorption of photons by the anode material with the larger intensity of the beam located towards the cathode. An image created using these X-ray reflects the spatial non-uniformity of the intensity and the variation of the effective focal spot size and shape across the X-ray beam.

III. DEVICE CHARACTERIZATION

A. Cathode Characterization

Current-voltage (I-V) characterization of the field emission chips is conducted inside an ultra-high vacuum chamber with pressure down to 5×10^{-10} Torr. A picture and a schematic of the setup are shown in Figure 6. A wafer covered with field emission chips is placed on a movable stage, which is connected to a Keithley 237 source-measure unit (SMU) to

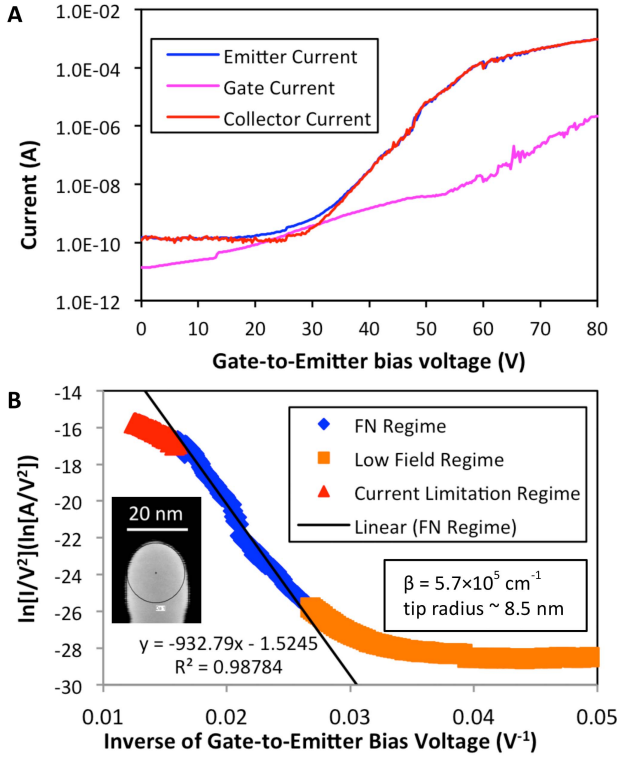


Fig. 7. Results of field emission tests on a column of field emitters: (a) current-voltage characteristics, (b) Fowler-Nordheim plot with inset of emitter tip radius.

supply a negative bias voltage to the substrate/emitter tips. Test probes are used to make contact to the gates, and the gates are grounded using a picoammeter Keithley 6485, so that the leakage/intercepted current can be measured. A phosphor screen is mounted 2 cm above the wafer top surface, serving as a collector and as electron spot imager. The phosphor screen is positively biased at 1000 V with a second Keithley 237 SMU.

During the I-V characterization, the emitter voltage is swept between 0 V and -80 V while measuring the emitter current, the collector current and the gate current. A typical I-V curve at ultra-high vacuum (Figure 7(a)) shows that the field emitter cathode turns on at ~ 25 V, and that almost all the current emitted from the tips is transmitted to the collector. Such low turn-on voltage is comparable to other silicon-tip field emitters reported in [22] and [28]–[30], and is much lower than CNT field emitters reported in [15] and [18] which turn on at over 500 V. We also observe that the gate current is dominated by current leakage through the dielectric instead of field emitted current that is intercepted by the gate structure, as the curve of the gate current does not follow the curves of the emitter current and the collector current.

In the Fowler-Nordheim (F-N) model [45], [46], the current I_E emitted from a tip biased at a voltage V_G is [13]

$$I_E(V_G) = \alpha_{tip} \frac{A_{FN}}{\phi^2(y)} E_{local}^2(V_G) \exp\left[\frac{-B_{FN}\phi^{3/2}}{E_{local}(V_G)} v(y)\right] \quad (1)$$

where α_{tip} is the emitting area of the tip, ϕ is the work-function of the tip, E_{local} is the local electrostatic field at the emitter tip, and A_{FN} and B_{FN} are universal constants

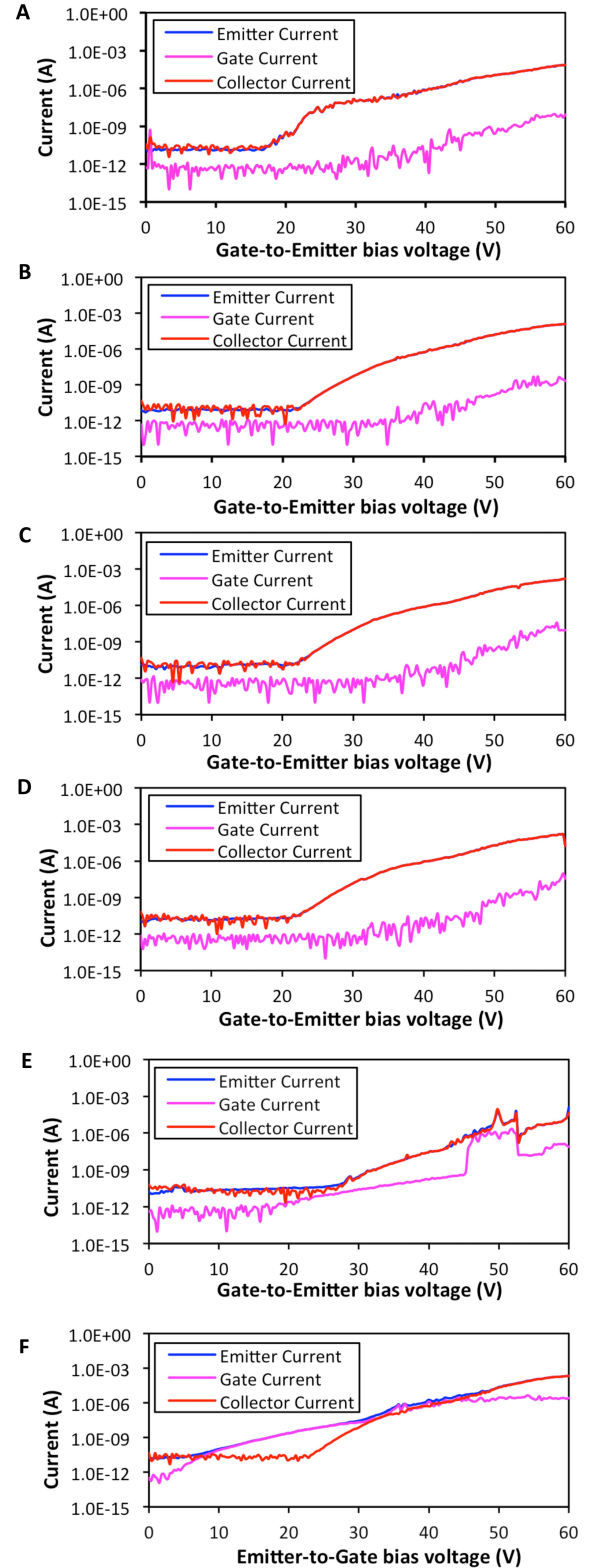


Fig. 8. I-V characteristics of the field emission cathode at different background pressures: (a) 5×10^{-9} Torr, (b) 5×10^{-8} Torr, (c) 5×10^{-7} Torr, (d) 5×10^{-6} Torr, (e) 5×10^{-5} Torr, and (f) back to 5×10^{-9} Torr.

equal to

$$A_{FN} = \frac{q^3}{8\pi h} = 1.54 \times 10^{-6} \left[AeV/V^2 \right] \quad (2)$$

$$B_{FN} = \left(\frac{8\pi}{3}\right) \frac{\sqrt{2m_e}}{qh} = 6.83 \times 10^7 \left[eV^{-3/2} V/cm \right] \quad (3)$$

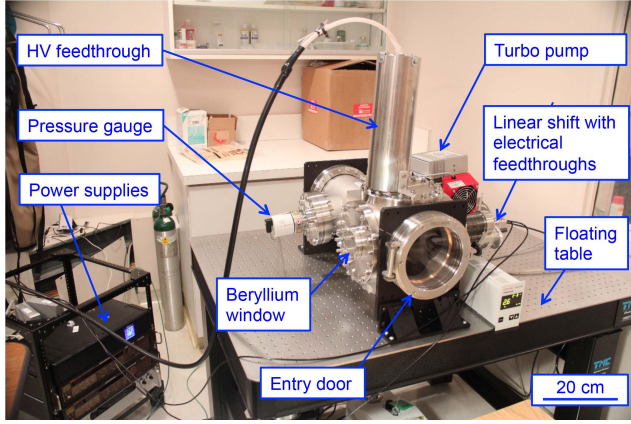


Fig. 9. Picture of the X-ray source.

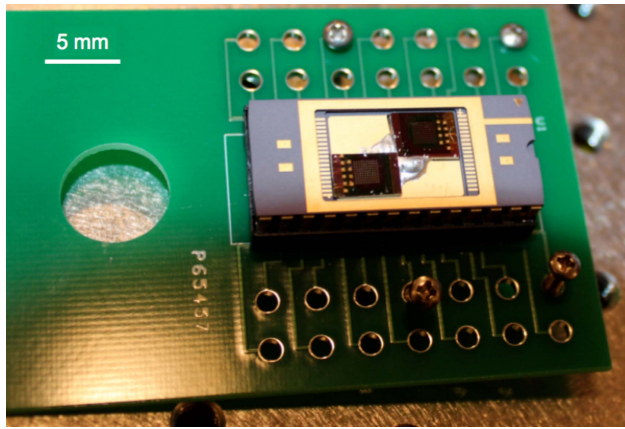


Fig. 10. Picture of packaged field emission cathodes.

where q is the electronic charge, h is Plank's constant, and m_e is the electron's effective mass, and $t(y)$ and $v(y)$ are the Nordheim elliptic functions where

$$y = \sqrt{\frac{q^3 E_{local}}{4\pi \epsilon_0 \phi^2}} \quad (4)$$

and ϵ_0 is the electrical permittivity of free space. The Nordheim elliptic functions can be approximated as $t(y) = 1.1$ and $v(y) = 0.95 - y^2$ [47]. The local electric field is related to the applied voltage V_G through $E_{local}(V_G) = \beta \cdot V_G$ where β is the field factor. Therefore, if we also assume that the emitter is at low temperature and it is made of a material with high electrical conductivity, equation (1) can be rewritten as

$$I_E(V_G) = \alpha_{tip} \frac{1.27 \times 10^{-6}}{\phi} \beta^2 V_G^2 \times \exp \left[\frac{9.87}{\sqrt{\phi}} - \frac{6.53 \times 10^7 \phi^{3/2}}{\beta V_G} \right] \quad (5)$$

Equation (5), predicts a linear relationship between $\ln(I_E/V_G^2)$ and V_G^{-1} with slope $-6.53 \times 10^7 \cdot \phi^{3/2}/\beta$. The field factor β relates the bias voltage to the surface electrostatic field and it is to first order equal to the inverse of the tip radius r . A better estimate of the field factor of a sharp field

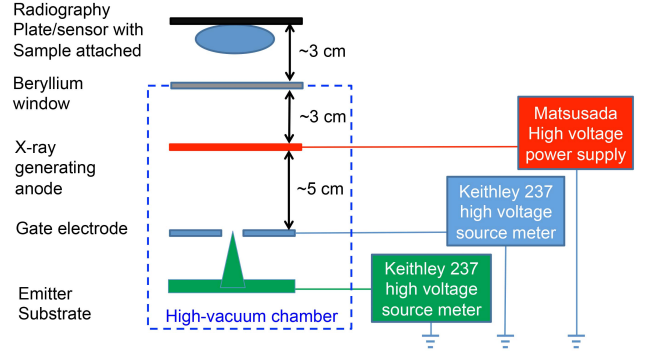
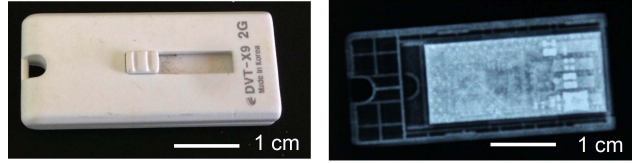
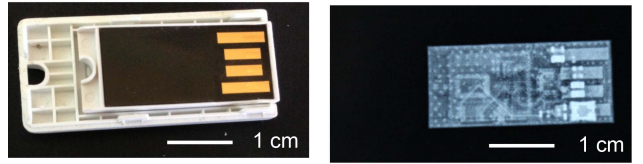


Fig. 11. Schematic of the table-top X-ray source setup.

3 pulses



5 pulses



10 pulses

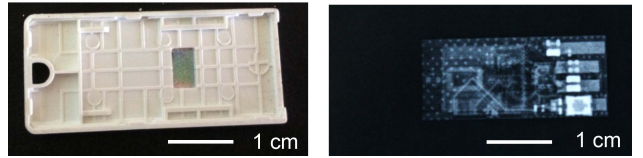


Fig. 12. X-ray images of a flash drive with varying dose.

emitter with proximal gate (i.e., an emitter with tip radii far smaller than the other dimensions of the emitter, and with gate-to-substrate separation of the order of the emitter height) is given by [22], [48]–[50]

$$\beta = \frac{k_F}{r^n} [cm^{-1}] \quad (6)$$

where $k_F \approx 2.5 \times 10^6$, $n \approx 0.69-0.8$, and r is the tip radius in nanometers. Figure 7(b) shows a typical F-N plot (i.e., $\ln(I_E/V_G^2)$ vs. V_G^{-1}) of the emitted current; from its slope, a field factor β equal to $5.7 \times 10^5 cm^{-1}$ is calculated with a workfunction for silicon of 4.05 eV. Based on the value of the field factor, we estimate that the emitter tip radius is ~ 8.5 nm if we use $n = 0.69$, which is close to measurements of the tip radii using SEM imaging, further corroborating that the current is field emitted (from SEM metrology of 50 tips selected at random we obtained an average tip radius of 10.4 nm and standard deviation of 0.8 nm; the standard deviation is in agreement with reported statistics of arrays of single-crystal silicon tips sharpened using long oxidation times [51]). The maximum current of 1 mA is obtained from ten 7 by 7 emitter arrays (a total of 490 field

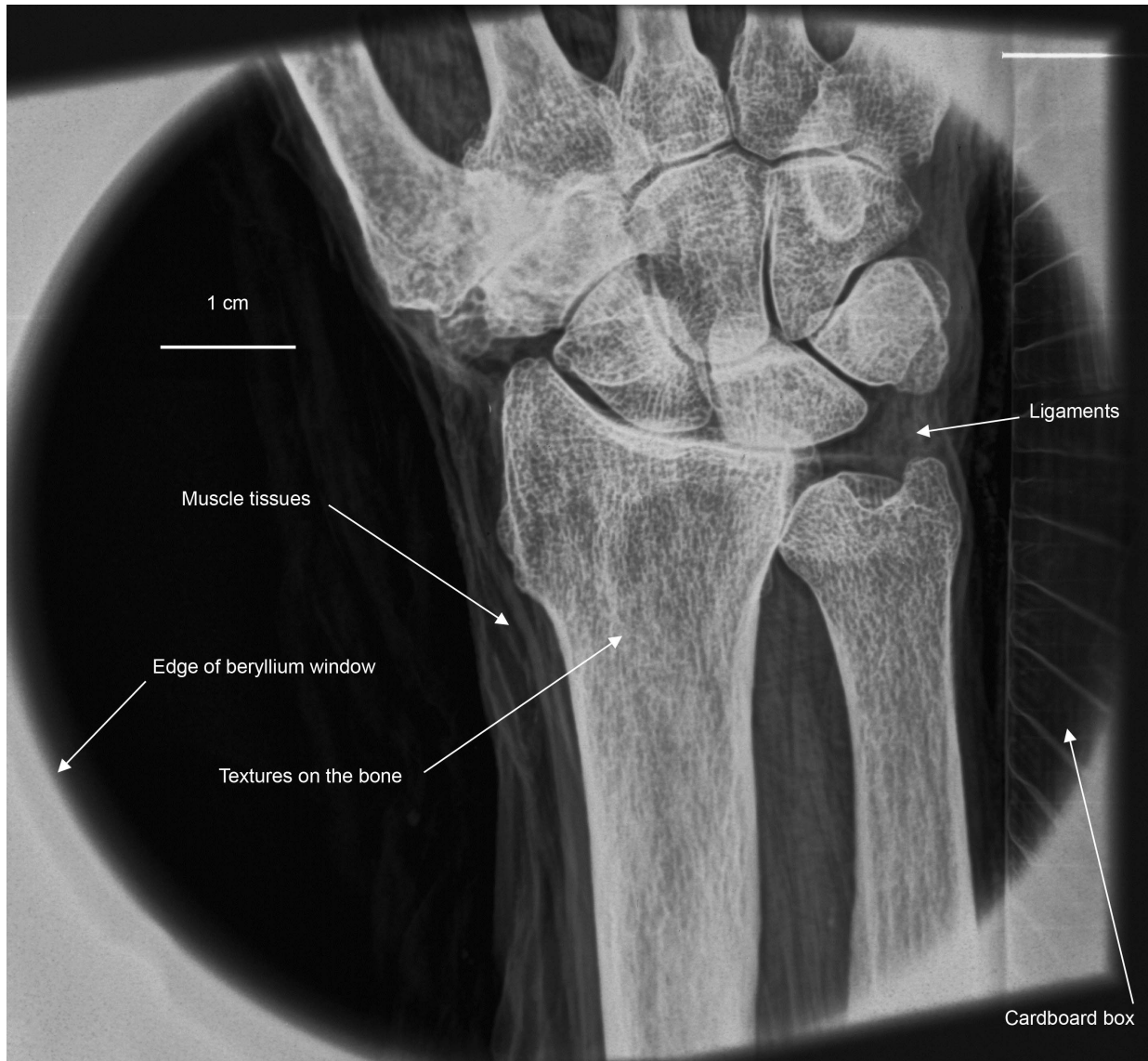


Fig. 13. X-ray image of an ex-vivo human wrist.

emitters); therefore, each emitter tip generates on average over $2 \mu\text{A}$ of electron current, significantly higher than the per-emitter currents from silicon FEAs previously reported [22], [28]–[30]. Since the spacing between two adjacent tips is $10 \mu\text{m}$, the current density of our FEAs is 2 A/cm^2 , which is also comparable or higher than the high-current-density CNT field emitters reported in [34]–[36]. However, the current per emitter is not large enough to produce emitter burnout because of the high thermal conductivity of silicon and because of the conic shape of the emitter tip with a rather wide base (see field emitter thermal model proposed by Utsumi [52]).

We also investigated the dependence of the I-V characteristics of the cathode on the background pressure. The background pressure can be varied in our testing rig by venting nitrogen into the chamber using a precision leak valve. Background pressures of 5×10^{-9} Torr, 5×10^{-8} Torr, 5×10^{-7} Torr, 5×10^{-6} Torr and 5×10^{-5} Torr were sequentially set; at each pressure level, gate-to-emitter voltages are swept between 0 V and 60 V. The I-V characteristics

at each background pressure are shown in Figure 8(a)–(e). The field emission cathode operates relatively stably at background pressures up to 5×10^{-6} Torr. Significant degradation of the I-V characteristics is observed at 5×10^{-5} Torr. The vacuum chamber is then pumped back to 5×10^{-9} Torr, and another I-V test is performed; the I-V curves at this pressure, shown in figure 8(f), indicate that the device has permanently degraded after operating at 5×10^{-5} Torr, resulting in much higher gate interception current.

B. X-Ray Generation Characterization

The implemented tabletop X-ray source is shown in Figure 9. The system has an 8-inch cubic vacuum chamber that contains the field emission cathode and the transmission anode. The chamber is maintained at a pressure of 2×10^{-8} Torr using a turbomolecular pump and a diaphragm pump. The cathode bias voltages are applied using a flange with a plurality of SHV-5 feedthroughs. The cathode holder is mounted onto

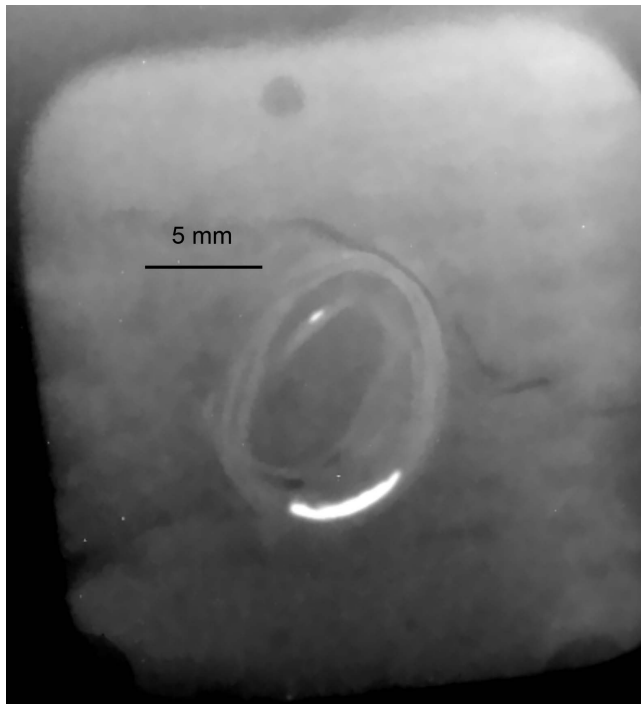


Fig. 14. X-ray image of a wax-coated iliac artery sample.

the same flange, which is connected to a linear positioning stage that is used to adjust the axial position of the cathode. The field emission cathodes are first metalized by e-beam evaporating 100 nm of gold on the contact pads; the wafer is then scribed and broken into individual dies. A standard dual in-line package (DIP) is used to hold two dies and gold wires are bonded to make electrical connections. The DIP is plugged into a socket that is soldered on a printed circuit board (PCB), as shown in Figure 10. The PCB is bolted to the cathode holder inside the vacuum chamber. The chamber has a high voltage feedthrough that allows biasing the anode up to 60 kV. A beryllium window is located behind the anode holder to transmit the X-ray emitted from the back of the anode to outside the chamber.

Figure 11 shows a schematic of the setup. The high voltage feedthrough for the anode is connected to a Matsusada high voltage power supply (AU80R15), capable of biasing up to 80 kV maximum and delivering up to 15 mA. The cathode gate and substrate (emitters) are connected to two Keithley 237 SMUs using SHV-5 feedthroughs. During the tests, the anode is biased at 15 to 40 kV, the gate voltage is fixed to 0 V, while negative pulses of one second are supplied to the emitter to emit approximately 600 μA of electron current pulses that are absorbed by the anode. A small digital X-ray detector (HandyCreate HDR-200, 22 lp/mm, pixel size 22.6 μm) is used to image small objects (up to $\sim 44 \times 32$ mm), and a 10" \times 12" computational radiographic plate (AGFA CR cassette, resolution $\sim 100\mu\text{m}$) is used for larger objects.

We imaged a number of inert samples to characterize the imaging capability of the X-ray system. For example, Figure 12 shows a series of absorption X-ray images of a flash drive with different exposure doses, i.e., number of 600 μA 1s-pulses while biasing the anode at 30 kV; these

images were captured using the small digital X-ray detector. The images clearly show features that are well under 1 mm in size. A smaller dose image provides more details of the plastic casing, while a larger dose image shows clearer profiles of the metal structures on the circuit board.

We also imaged a number of ex-vivo samples to demonstrate the capability of the system to capture detailed absorption X-ray images of soft tissue without any markers. One of the samples we imaged was an ex-vivo human wrist using a computation radiographic plate (Figure 13). This image was taken with 300 μA of current with 5 s total exposure time (1.5 mA.s) at 30 kV; this dose is much lower than what is typically used in clinical practice to image the same structure (40 mA.s at 60 kV [53]). The high-quality X-ray absorption image clearly shows soft tissue and fine bone structures. This image exhibits superior contrast and resolution compared to the images from the previously reported X-ray sources with a miniaturized field emission cathode and a reflection anode [14] or a transmission anode [54]; it also provides much more details than the state-of-the-art X-ray systems used in hospitals [55]. Furthermore, Figure 13 even shows the structure of the cardboard box that contained the ex-vivo sample (segmented vertical structure on the right side of the picture). We also imaged a wax-coated iliac artery specimen with extensive atherosclerotic plaque. The density of wax and tissue are fairly similar; therefore, in a standard absorption X-ray image the two structures should not be distinguishable. However, as shown in Figure 14, the cross section of the iliac artery wall can be clearly distinguished from the surrounding wax layer; in addition, the calcification of the artery can be seen as a white elongated feature on the bottom of the artery. Moreover, Figure 14 has striking similarity to an X-ray image of the same sample taken using advanced phase-contrast techniques that rely on coherent X-ray sources for their exposure [56]. Both Figures 13 and 14 demonstrate that the X-ray source can image rich details within the soft tissues and low-Z materials; this is usually difficult to achieve using conventional X-ray sources without the use of contrast agents such as iodine and barium.

We believe that the superior image quality is related to the near-monochromaticity of the X-ray radiation. The spectra of the X-ray emission were measured using an Amptek X-123 X-ray spectrometer at different anode voltages. The spectra are plotted in Figure 15. The two energy peaks at 9.713 keV and 11.442 keV correspond to the $L\alpha_1$ and $L\beta_1$ lines of gold, respectively. At 30 kV and 40 kV anode voltages, the relative intensity of the background radiation (bremsstrahlung) is much smaller than at 15 kV and 20 kV. The lower level of background radiation improves the monochromaticity of the X-ray, which may contribute to the clarity and sharpness of the image. For the transmission anode we used, the optimal bias voltage seems to be around 30 kV (maximization of the ratio of X-ray fluorescence over the total emission).

We designed the thickness of the X-ray generating material for 60 kV, i.e., the maximum anode bias voltage in our setup. We thought we would need the largest bias voltage to produce the best images; however, we obtained our best images of samples with soft tissue by biasing the anode at ~ 30 kV;

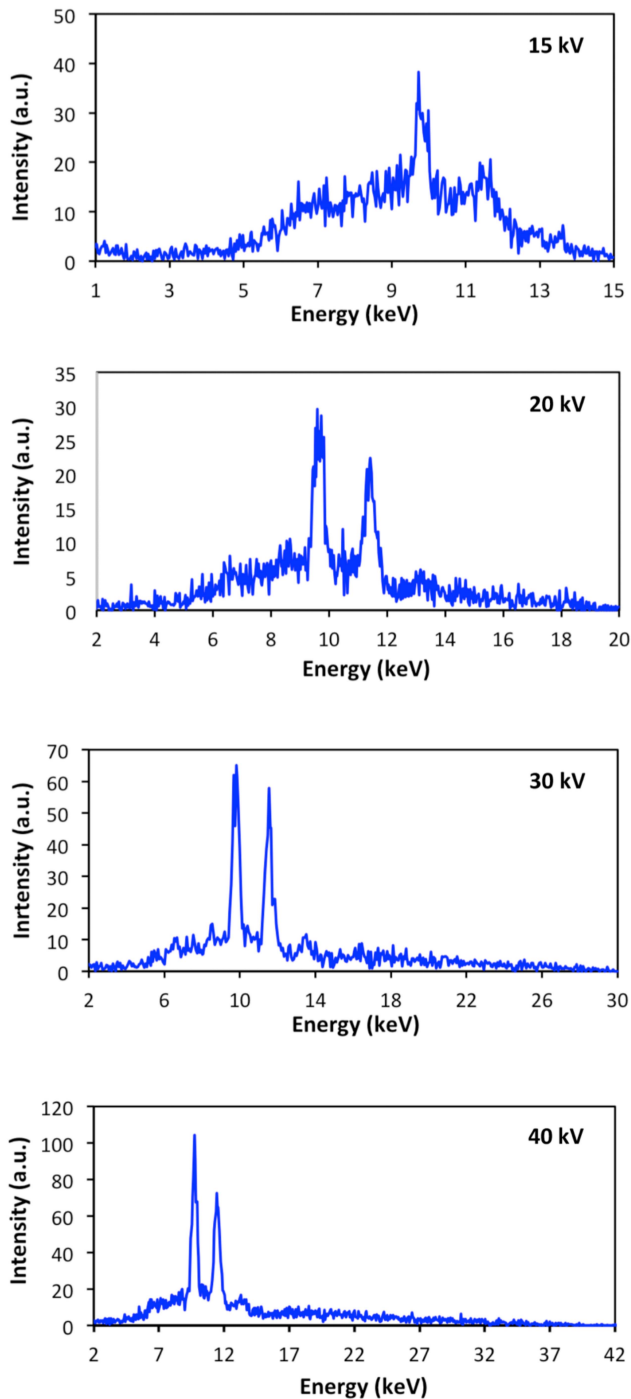


Fig. 15. Measured spectra of the X-ray radiation at different anode voltages.

in addition, the data suggest that the bias voltage that maximizes the ratio of X-ray fluorescence over the total emission is around 30 kV. Therefore, it is possible that by using an anode with a thinner X-ray generating material (designed using the actual operational anode bias voltage) the facility can produce better images. However, the extra thickness of the X-ray generating material is also acting as a filter of X-ray, possibly improving the ratio of the dual-peak emission over the total X-ray emission, which should help produce better images. Further investigation into the matter is required.

The X-ray source is currently operated in pulsed mode with low duty cycle to avoid increasing the pressure inside the chamber, which can result in destruction of the cathode due to back ion bombardment (see Figure 8). The chamber pressurization results from outgassing of the anode due to heating because only about 1% of the kinetic energy of the electrons impacting the anode is transformed into X-ray [57]. We typically produce 1-second current pulses with 4-second period and with a few pulses an image is obtained. Proper cooling of the anode needs to be addressed to be able to capture an image with only one multi-second pulse, and to be able to capture an arbitrary number of images with little time between exposures.

IV. CONCLUSION

A nanostructured silicon field emission cathode capable of low-voltage operation and high current emission with high gate transmission has been demonstrated. A proof-of-concept X-ray source has been built with the field emission cathode and a microstructured transmission anode. The X-ray source generates radiation that allows clear imaging of low-Z materials, in particular of biological samples. The spectrum analysis of the X-ray shows lower background radiation due to the filtering effect of the transmission anode and the efficient X-ray generation of the transmission anode, as well as emission of X-ray with narrow spectral linewidth.

ACKNOWLEDGMENT

The field emission cathodes and the transmission anodes were fabricated at the Microsystems Technology Laboratories of the Massachusetts Institute of Technology. The authors would like to thank R. Gupta from Massachusetts General Hospital (MGH) for providing the space at MGH Navy Yard to install the X-ray generator, supplying the ex-vivo samples, and for helping acquire the X-ray absorption images. Any opinions, findings, and conclusions or recommendations expressed in this publication are those of the authors and do not necessarily reflect the views of the US Government and therefore, no official endorsement of the US Government should be inferred.

REFERENCES

- [1] C. K. Eun and Y. B. Gianchandani, "A microfabricated steel and glass radiation detector with inherent wireless signaling," *J. Micromech. Microeng.*, vol. 21, no. 1, pp. 015003-1–015003-10, 2011.
- [2] S. M. Pellegrin, C. Whitney, and C. G. Wilson, "A multichannel nanoparticle scintillation microdevice with integrated waveguides for alpha, beta, gamma, X-ray, and neutron detection," *J. Microelectromech. Syst.*, vol. 19, no. 5, pp. 1207–2214, 2010.
- [3] G. C. Giakos *et al.*, "An efficient, novel microstrip collector architecture for digital radiographic imaging CZT semiconductor sensors," *IEEE Trans. Instrum. Meas.*, vol. 54, no. 3, pp. 1144–1149, Jun. 2005.
- [4] A. Swawant *et al.*, "Segmented phosphors: MEMS-based high quantum efficiency detectors for megavoltage X-ray imaging," *Med. Phys.*, vol. 32, no. 2, pp. 553–565, 2005.
- [5] I. Mitsuishi *et al.*, "Novel ultra-lightweight and high-resolution MEMS X-ray optics for space astronomy," *Sens. Actuators A, Phys.*, vol. 188, pp. 411–416, Dec. 2012.
- [6] Y. Shi and A. Lal, "Integrated all-electric high energy ion beam guidance on chip: Towards miniature particle accelerator," in *Proc. 24th Int. Conf. Micro Electro Mech. Syst. (MEMS)*, Jan. 2011, pp. 137–140.

- [7] P. Rangsten, C. Ribbing, C. Strandman, B. Hök, and L. Smith, "Field-emitting structures intended for a miniature X-ray source," *Sens. Actuators A, Phys.*, vol. 82, nos. 1–3, pp. 24–29, May 2000.
- [8] M. Azad, D.-O. Choe, and H. Kim, "Mini X-ray imaging based on safely shielded pure beta radioisotopes," in *Proc. 26th Int. Conf. Micro Electro Mech. Syst. (MEMS)*, Taipei, Taiwan, Jan. 2013, pp. 1101–1104.
- [9] B. Beckhoff, B. Kanngießner, N. Langhoff, R. Wedell, and H. Wolff, *Handbook of Practical X-Ray Fluorescence Analysis*. New York, NY, USA: Springer, 2006.
- [10] S. Cheng, F. A. Hill, E. V. Heubel, and L. F. Velásquez-García, "A compact X-ray generator using a nanostructured field emission cathode and a microstructured transmission anode," in *J. Phys., Conf. Ser.*, Dec. 2013, vol. 476, no. 1, p. 012016.
- [11] W. I. Milne *et al.*, "Carbon nanotubes as field emission sources," *J. Mater. Chem.*, vol. 14, no. 6, pp. 933–943, 2004.
- [12] C. M. Slack and L. F. Ehrke, "Field emission X-ray tube," *J. Appl. Phys.*, vol. 12, no. 2, pp. 165–168, Feb. 1941.
- [13] R. Gomer, *Field Emission and Field Ionization*. New York, NY, USA: Springer, 1993.
- [14] S. Kita *et al.*, "Field-emission-type X-ray source using carbon-nanofibers," *J. Appl. Phys.*, vol. 103, no. 6, p. 064505, Mar. 2008.
- [15] S. Wang, X. Calderon, R. Peng, E. C. Schreiber, O. Zhou, and S. Chang, "A carbon nanotube field emission multipixel X-ray array source for microradiotherapy application," *Appl. Phys. Lett.*, vol. 98, no. 21, p. 213701, May 2011.
- [16] H. Y. Choi, J. U. Kim, and C. J. Lee, "Development of carbon nanotube based reflection type X-ray source," *Acta Phys. Polonica Ser. A General Phys.*, vol. 115, no. 6, pp. 1078–1080, Jun. 2009.
- [17] J. Koohsorkhi, S. Mohajerzadeh, and S. Darbari, "Investigation of carbon nanotube-based field-emission triode devices on silicon substrates," *IEEE Trans. Nanotechnol.*, vol. 11, no. 6, pp. 1252–1258, Nov. 2012.
- [18] B. Diop and V. T. Binh, "Quasi-monochromatic field-emission X-ray source," *Rev. Sci. Instrum.*, vol. 83, no. 9, p. 094704, Sep. 2012.
- [19] T. Tyler, O. A. Shenderova, and G. E. McGuire, "Vacuum microelectronic devices and vacuum requirements," *J. Vac. Sci. Technol. A*, vol. 23, no. 4, pp. 1260–1266, Jul. 2005.
- [20] C. A. Spindt, "A thin-film field-emission cathode," *J. Appl. Phys.*, vol. 39, no. 7, pp. 3504–3505, Jun. 1968.
- [21] F. Ceccanti, S. Marcuccio, M. Andrenucci, and C. A. Srl, "FEFP thruster survivability in the LEO atomic oxygen environment," in *Proc. 27th Int. Electr. Propuls. Conf. (IEPC)*, Pasadena, CA, USA, Oct. 2001, no. IEPC-01-295, pp. 1–13.
- [22] M. Ding, G. Sha, and A. I. Akinwande, "Silicon field emission arrays with atomically sharp tips: Turn-on voltage and the effect of tip radius distribution," *IEEE Trans. Electron Devices*, vol. 49, no. 12, pp. 2333–2342, Dec. 2002.
- [23] M. O. S. Dantas, E. Galeazzo, H. E. M. Peres, M. M. Kopelovski, and F. J. Ramirez-Fernandez, "Silicon field-emission devices fabricated using the hydrogen implantation-porous silicon (HI-PS) micromachining technique," *J. Microelectromech. Syst.*, vol. 17, no. 5, pp. 1263–1269, 2008.
- [24] K. Sun *et al.*, "Field emission tip array fabrication utilizing geometrical hindrance in the oxidation of Si," *IEEE Trans. Nanotechnol.*, vol. 11, no. 5, pp. 999–1003, Sep. 2012.
- [25] J. Browning, "Field emission display development and testing," in *Proc. Int. Vac. Microelectron. Conf.*, Jul./Aug. 1995, pp. 1–7.
- [26] T. S. Ravi, R. B. Marcus, and D. Liu, "Oxidation sharpening of silicon tips," *J. Vac. Sci. Technol. B, Microelectron. Nanometer Struct.*, vol. 9, no. 6, pp. 2733–2737, Nov. 1991.
- [27] D. Temple, "Recent progress in field emitter array development for high performance applications," *Mater. Sci. Eng. R, Rep.*, vol. 24, no. 4, pp. 185–239, Jan. 1999.
- [28] E. A. Adler, Z. Bardai, R. Forman, D. M. Goebel, R. T. Longo, and M. Sokolich, "Demonstration of low voltage field emission," *IEEE Trans. Electron Devices*, vol. 38, no. 10, pp. 2304–2308, Oct. 1991.
- [29] J. T. Trujillo, A. Chakhovskoi, and C. E. Hunt, "Low voltage silicon field emitters with gold gates," in *Proc. Int. Vac. Microelectron. Conf.*, Jul./Aug. 1995, pp. 42–46.
- [30] K. Koga, K. Morimoto, Y. Hori, S. Kanemaru, and J. Itoh, "New structure Si field emitter arrays with low operation voltage," in *Tech. Dig. Int. Electron Devices Meet.*, Dec. 1994, pp. 23–26.
- [31] L. M. Baskin and G. N. Fursey, "Field emission from semiconductors," in *Proc. Int. Vac. Microelectron. Conf.*, Jul./Aug. 1995, p. 66.
- [32] L. F. Velásquez-García, S. A. Guerrero, Y. Niu, and A. I. Akinwande, "Uniform high-current cathodes using massive arrays of Si field emitters individually controlled by vertical Si ungated FETs—Part 1: Device design and simulation," *IEEE Trans. Electron Devices*, vol. 58, no. 6, pp. 1775–1782, Jun. 2011.
- [33] L. F. Velásquez-García, S. A. Guerrero, Y. Niu, and A. I. Akinwande, "Uniform high-current cathodes using massive arrays of Si field emitters individually controlled by vertical Si ungated FETs—Part 2: Device fabrication and characterization," *IEEE Trans. Electron Devices*, vol. 58, no. 6, pp. 1783–1791, Jun. 2011.
- [34] H. Mu, X. Zhang, W. Lei, C. Lou, Q. Wang, and X. Yin, "High-current-density field emission from multiwalled carbon nanotubes by chemical-vapor deposition with effective aging treatment," *J. Vac. Sci. Technol. B, Microelectron. Nanometer Struct.*, vol. 25, no. 2, pp. 583–585, Mar. 2007.
- [35] P. Serbun, G. Muller, A. Tymoshchuk, I. Kashko, B. Shulitski, and V. Labunov, "High field emission current density from structured CNT bundle cathodes," in *Proc. 26th Int. Vac. Nanoelectron. Conf.*, Jul. 2013, pp. 1–2.
- [36] L. Wei, X. Zhang, J. Chen, Z. Zhao, Y. Cui, and B. Wang, "Very high field emission from a carbon nanotube array with isolated subregions and balanced resistances," *IEEE Trans. Electron Devices*, vol. 58, no. 10, pp. 3616–3621, Oct. 2011.
- [37] A. A. Fomani, A. I. Akinwande, and L. F. Velásquez-García, "Resilient, nanostructured, high-current, and low-voltage neutralizers for electric propulsion of small spacecraft in low earth orbit," in *J. Phys., Conf. Ser.*, 2013, vol. 476, no. 1, p. 012014.
- [38] F. E. Carroll, M. H. Mendenhall, R. H. Traeger, C. Brau, and J. W. Waters, "Pulsed tunable monochromatic X-ray beams from a compact source: New opportunities," *Amer. J. Roentgenol.*, vol. 181, no. 5, pp. 1197–1202, Nov. 2003.
- [39] Y. Aglitskiy *et al.*, "High-resolution monochromatic X-ray imaging system based on spherically bent crystals," *Appl. Opt.*, vol. 37, no. 22, pp. 5253–5261, Aug. 1998.
- [40] D. B. Sinars *et al.*, "Monochromatic X-ray imaging experiments on the Sandia national laboratories Z facility," *Rev. Sci. Instrum.*, vol. 75, no. 10, pp. 3672–3677, Oct. 2004.
- [41] R. T. Lopes, E. B. Costa, and E. F. O. de Jesus, "Computed tomography with monochromatic bremsstrahlung radiation," *Appl. Radiat. Isotopes*, vol. 53, no. 4, pp. 665–671, Oct./Nov. 2000.
- [42] G. G. Poludniowski, "Calculation of X-ray spectra emerging from an X-ray tube. Part II. X-ray production and filtration in X-ray targets," *Med. Phys.*, vol. 34, pp. 2175–2186, Jun. 2007.
- [43] G. Harding, B. David, A. Harding, A. Thran, and J. P. Schlomka, "Directional enhancement of characteristic relative to bremsstrahlung X-rays: Foil thickness optimization," *Radiat. Phys. Chem.*, vol. 76, no. 7, pp. 1116–1121, Jul. 2007.
- [44] D. Drouin, A. R. Couture, D. Joly, X. Tastet, V. Aimez, and R. Gauvin, "Casino V2.42—A fast and easy-to-use modeling tool for scanning electron microscopy and microanalysis users," *Scanning*, vol. 29, no. 3, pp. 92–101, 2007.
- [45] R. H. Fowler and L. W. Nordheim, "Electron emission in intense electric fields," *Proc. Roy. Soc. A*, vol. 119, no. 781, pp. 173–181, May 1928.
- [46] L. W. Nordheim, "The effect of the image force on the emission and reflection of electrons by metals," *Proc. Roy. Soc., A*, vol. 121, no. 788, pp. 626–639, 1928.
- [47] I. Brodie and C. Spindt, *Advances in Electronics and Electron Physics*. New York, NY, USA: Academic, 1992, pp. 1–106.
- [48] L. Dvorson, G. Sha, I. Kymissis, C.-Y. Hong, and A. I. Akinwande, "Electrical and optical characterization of field emitter tips with integrated vertically stacked focus," *IEEE Trans. Electron Devices*, vol. 50, no. 12, pp. 2548–2558, Dec. 2003.
- [49] L. Dvorson, M. Ding, and A. I. Akinwande, "Analytical electrostatic model of silicon conical field emitters. I," *IEEE Trans. Electron Devices*, vol. 48, no. 1, pp. 134–143, Jan. 2001.
- [50] L. Dvorson, M. Ding, and A. I. Akinwande, "Analytical electrostatic model of silicon conical field emitters. II. Extension to devices with focusing electrode," *IEEE Trans. Electron Devices*, vol. 48, no. 1, pp. 144–148, Jan. 2001.
- [51] M. E. Swanwick, P. D. Keathley, F. X. Kärtner, and L. F. Velásquez-García, "Ultrafast photo-triggered field emission cathodes using massive, uniform arrays of nano-sharp high-aspect-ratio silicon structures," in *Tech. Dig. 17th Int. Conf. Solid-State Sens., Actuators, Microsyst.*, Barcelona, Spain, Jun. 2013, pp. 2680–2683.

- [52] T. Utsumi, "Keynote address -Vacuum microelectronics: What's new and exciting," *IEEE Trans. Electron Devices*, vol. 38, no. 10, pp. 2276–2283, Oct. 1991.
- [53] J. T. Bushburg, J. A. Seibert, E. M. Leidholdt, and J. M. Boone, *The Essential Physics of Medical Imaging*, 3rd ed. New York, NY, USA: Lippincott Williams & Williams, 2011, pp. 202–206.
- [54] Y. Zingerman, H. Golan, A. Gersten, and A. Moalem, "A compact CT/SPECT system for small-object imaging," *Nucl. Instrum. Methods Phys. Res. A, Accel. Spectrometers Detectors Assoc. Equip.*, vol. 584, pp. 135–148, Jan. 2008.
- [55] (2014, May 17). *American Society for Surgery of the Hand* [Online]. Available: <http://www.assh.org/Public/HandConditions/Pages/WristSprains.aspx>
- [56] M. Ando *et al.*, "Crystal analyser-based X-ray phase contrast imaging in the dark field: Implementation and evaluation using excised tissue specimens," *Eur. Radiol.*, vol. 24, no. 2, pp. 423–433, 2014.
- [57] A. B. Worlbarst, *Physics of Radiology*. Madison, WI, USA: Medical Phys. Publishing, 2005.



Frances Ann Hill received the B.A.S. degree from the University of Waterloo, Waterloo, ON, Canada, in 2006, and the M.S. and Ph.D. degrees from the Department of Mechanical Engineering, Massachusetts Institute of Technology (MIT), Cambridge, MA, USA, in 2008 and 2011, respectively. From 2011 to 2013, she was a Post-Doctoral Associate with the Microsystems Technology Laboratories at MIT. She is currently a Research Scientist with KLA-Tencor Corporation, Milpitas, CA, USA.



Eric Vincent Heubel received the B.S. degree from the Department of Mechanical Engineering, Michigan Technological University, Houghton, MI, USA, in 2006, and the M.S. degree from the Department of Mechanical Engineering, Massachusetts Institute of Technology, Cambridge, MA, USA, in 2008, where he is currently pursuing the Ph.D. degree focusing on precision micromachined plasma sensors.



Shuo Cheng received the B.S. degree in automation from the Beijing Institute of Technology, Beijing, China, in 2006, and the M.S. and Ph.D. degrees in electrical and computer engineering from the University of Florida, Gainesville, FL, USA, in 2011.

He was a Post-Doctoral Associate with the University of Florida, and Microsystems Technology Laboratories, Massachusetts Institute of Technology, Cambridge, MA, USA, from 2012 to 2014. He is currently a Research Engineer with Stellarray Inc., Austin, TX, USA.



Luis Fernando Velásquez-García (M'09–SM'10) is a Principal Scientist with the Microsystems Technology Laboratories, Massachusetts Institute of Technology, Cambridge, MA, USA. His research focuses on micro and nanoenabled multiplexed scaled-down systems for space, energy, healthcare, manufacturing, and analytical applications that exploit high-electric field phenomena, e.g., electro-spray, electrospinning, electron impact ionization, field emission, field ionization, plasmas, and X-ray.